Linker-Derived Contortion Controls Performance in Organic Polymer Pseudocapacitors

Jesse Gray,[†] Victoria A. Posey,[†] Nicholas M. Orchanian, Zexin Jin, Michael L. Steigerwald,[*] Xavier Roy,[*] and Colin Nuckolls[*]

Department of Chemistry, Columbia University, New York, New York 10027, United States

Abstract: Pseudocapacitors offer a unique strategy to combine the rapid charging rates of a capacitor with the high energy density of a battery, potentially offering a unique solution to energy storage challenges. Bending, twisting, and generally deplanarizing aromatic building blocks to form contorted aromatics has emerged as a new strategy to create organic materials with unique and tunable properties. This manuscript studies the union between these two concepts: molecular contortion and organic pseudocapacitors. The recent development of fully-organic pseudocapacitors, including high-performing devices based on perylene diimide organic redox units, introduces the added benefit of low cost, synthetic tunability, and increased flexibility. We synthesize a series of polymers by joining perylene diimide with various linkers which incorporate a helical moiety from [4]helicene to [6]helicene into the molecular backbone. We prepare three new electroactive polymers that incorporate benzene, naphthalene, and anthracene linkers and studied their pseudocapacitive performance to infer key design principles for organic pseudocapacitors. Our results show that the naphthalene linker results in the most strongly-coupled redox centers and displays the highest pseudocapacitance of 292 ± 47 F/g at 0.5 A/g. To understand

the pseudocapacitive behavior, we synthesize dimer model compounds to further probe the electronic structure of these materials through electronic absorption spectroscopy and first-principles calculations. Our results suggest that the identity of the aromatic linker influences the contortion between neighboring perylene diimide units, the coupling between redox centers, and their relative angles and distances. We find that competing molecular design factors must be carefully optimized to generate high-performance devices. Overall, this study provides key insights into molecular design strategies for generating high-performing organic pseudocapacitor materials.

Introduction

The increasing electrification of the modern world has led to growing demands for improved energy storage systems. The proliferation of personal electronics, electric vehicles, and electric aircraft is largely enabled by metal-ion battery technologies. However, battery materials continue to suffer from fundamental energy density limits, sluggish charging/discharging rates, and thermal runaway issues.[1,2] Furthermore, batteries typically rely on metal oxide materials that prevent the development of flexible energy storage devices and in many cases contain expensive elements.[3] Pseudocapacitors offer unique benefits as charge storage materials because they combine the high energy densities of batteries with the high-power densities of capacitors.[4–6] While a majority of high-performance pseudocapacitors are based on metal oxide materials, the recent development of advanced organic pseudocapacitors (in particular those incorporating conducting polymers) has enabled the production of devices that are economical, sustainable, high performing and with a diversity of form factors.[7,8] Perylene diimide (PDI) derivatives are a stable, tunable, and low-cost building block to construct organic pseudocapacitor materials with extraordinary properties.[9–11] Previous studies explored coupling PDI redox sites through a triptycene linker, resulting in a

conducting polymer with stable pseudocapacitance for >10,000 cycles.[9] The high performance of these devices was attributed to the three-dimensional structure imposed by the triptycene core and its high internal surface area, though the specific influence of the linker structure on the observed electrochemical properties remains unexplored.

In this study, we design a series of PDI-based building blocks with variable conjugated linkers to elucidate the design principles for helically contorted moieties in pseudocapacitor devices. We create and compare three new polymers by systematically varying the linker length, from benzene, to naphthalene, and anthracene (Figure 1), with the added benefit of including a helical moiety from [4]helicene to [6]helicene into the molecular backbone. These materials offer a platform to study the impact of linker length, conjugation, and the coupling between redox sites as they decrease in distance due to the helical contortion. Electrochemical measurements of these polymers indicate that the polymer containing the naphthalene linker (p-NPH) exhibits the optimal performance, with the highest pseudocapacitance in the series at 292 ± 47 F/g at 0.5 A/g, while also being the most contorted with the [6]helicene backbone, resulting in the greatest coupling between redox centers. To further understand the structure-properties relationship in these materials, we synthesize small-molecule dimer models with varying conjugation, length, and helicity. We probe the electronic structure of these materials through electronic absorption spectroscopy, cyclic voltammetry, and DFT calculations.

Results and Discussion

Preparation of pseudocapacitive polymers. We synthesize the polymers p-BZ, p-NPH, and p-ANH, where p stands for polymer and -BZ, -NPH, -ANH indicates benzene, naphthalene and anthracene, respecitvely. These polymers are prepared through Suzuki coupling followed by photocyclization onto the bay-region of PDI (Figure 1).[12] The photocyclization to form the

helicene subunits of the PDI core increases the rigidity and aromatic surface area of the polymers.[9] The preparation of the dibromo-PDI and the respective borylated linkers is described in Reaction Scheme S1-3, S6-8, S11-13. The dibromo-PDI core contains branched C-11 alkyl chains to improve the solution processability of these materials. We characterize the polymers via mass spectrometry and ^{1}H-NMR, comparing characteristic peaks to that of dimeric materials, and then remove the alkyl chains to increase porosity and conductivity through thermolysis to yield insoluble powders (Figure S4-7, S10-15).[9,10] We characterize these insoluble materials with TGA, FT-IR, and CO_2 adsorption analysis to confirm their identity and properties prior to device-level studies.

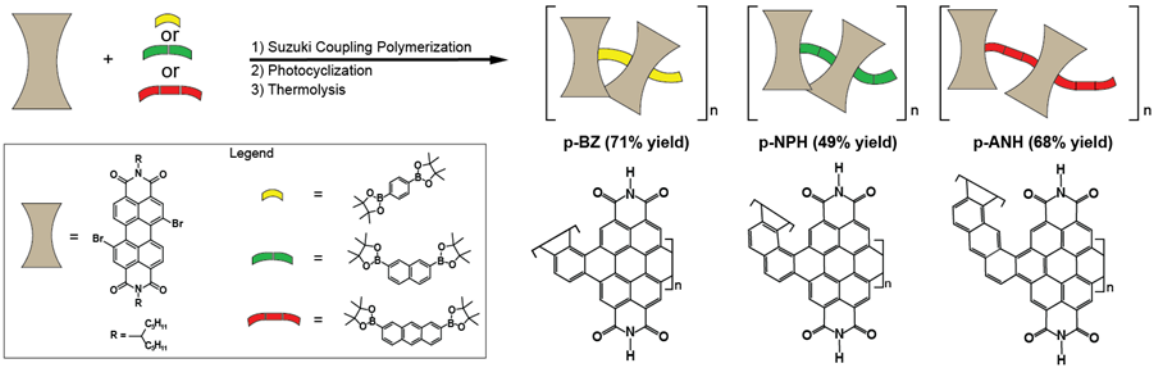

Figure 1. Synthesis of the PDI polymers using a Suzuki coupling and photocyclization to form the structures shown on the bottom right. The box inset shows the starting materials in the synthesis with the polymer p-BZ linked via benzene, p-NPH linked via naphthalene, and p-ANH linked via anthracene.

Electrochemistry and Pseudocapacitance Studies. To evaluate the electrochemical performance of these polymers, we first prepare a slurry containing carbon black, polytetrafluoroethylene (PTFE), and the active material (1:1:8 mass ratio) in *N*-methyl-2-pyrrolidone. We next drop cast the slurry onto carbon paper and vacuum dry (see Supporting

Information for additional details) to form the working electrode. Finally, we soak the working electrodes in 5 M NaCl solution under vacuum for 1 h to ensure full permeation of the porous material. Figure 2a,b displays the cyclic voltammetry (CV) and galvanostatic charge-discharge (GCD) studies for each polymer. Taken together these data establish the pseudocapacitive nature of these polymers. While PDI, the parent compound, is known to undergo two single-electron reduction events centered on the imides, the cyclic voltammograms for these polymers each display a single, broad, multi-electron reduction.[9,10] We measure half-wave potentials ($E^0_{1/2}$) for these materials of −0.68, −0.66 and −0.76 V for p-BZ, p-NPH and p-ANH, respectively, indicating that the extended, π-electron rich anthracene linker destabilizes reduction of p-ANH. Analyses of the scan rate dependence of the CV profiles reveals pseudocapacitive behavior for these materials (see the Supporting Information for details), which is further corroborated by the triangular shape of the GCD curves (Figure 2b). The specific capacitance (C_S) in Figure 2c can be calculated from the GCD according to the following equation:

$$C_S = \frac{I \times t}{m \times \Delta E}$$

where I is the current, t is the discharging time, m is the mass and ΔE is the potential difference for the discharge process. From this data measured across multiple devices, we find that p-NPH exhibits the highest pseudocapacitance at 292 ± 47 F/g, followed by p-BZ at 250 ± 34 F/g, and p-ANH at 147 ± 18 F/g (at a cycling rate of 0.5 A/g).

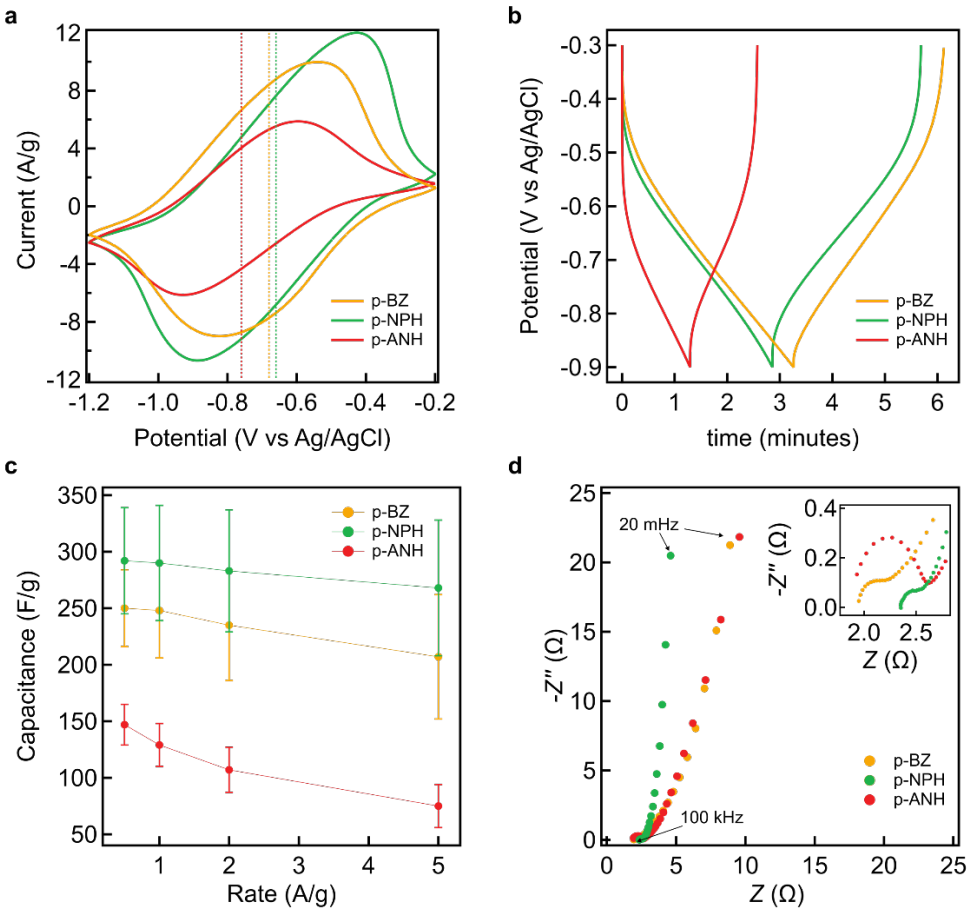

Figure 2. (a) Cyclic voltammograms of the PDI polymers measured at a scan rate of 30 mV/s with the half-wave potential shown as a dashed line in the respective color for each polymer. (b) GCD curves measured at 1 A/g. (c) Specific capacitance as a function of scan rate. (d) Nyquist plot from 100 kHz to 20 mHz. Inset: small semicircles at high frequencies. Measurements in (a-d) were performed in a three-electrode set up in 5 M aqueous NaCl.

To probe the ion diffusion behavior and its relation to the differences in pseudocapacitance, we perform electrochemical impedance spectroscopy (EIS) (Figure 2d) and galvanostatic intermittent titration technique (GITT) (Figure S32). Figure 2d shows the Nyquist plots measured at the half-peak potential of each polymer, which display semicircles in the high frequency regions, where the x-axis intercept is attributed to the equivalent series resistance (ESR) of the system and the

diameter is the charge-transfer resistance (R_{CT}) (see SI for a model of the circuit).[13,14] The ESR values across the series show a slight variation with values of 1.95, 2.35, and 1.93 Ω for p-BZ, p-NPH and p-ANH, respectively. The R_{CT} value also shows a small change from 0.68 Ω in p-ANH to 0.25 Ω for p-BZ and 0.20 Ω for p-NPH. Further analysis of the polymers show that the increased length of the linker bridge does not affect the diffusion coefficient obtained from GITT (Table S1) as ion mobilities on the order of 10^{-7} cm^2 s^{-1} are measured across the series. In addition, we explore CO_2 adsorption analysis on each of the polymers which shows increased adsorption and BET surface area for p-NPH compared to p-BZ and p-ANH (Figure S33, Table S1). This increased adsorption as derived from the helical structural motif is suggestive of a more open structure for better ion diffusion though not manifested in the diffusion coefficient and ion mobility. Overall, the CV, EIS, and CO_2 adsorption analysis results highlight key differences in the electrochemical behavior of these materials, demonstrating the critical role of molecular design on device-level performance. In particular, we find that the extended anthracene linker in p-ANH destabilizes the PDI reduction events (by 100 mV relative to p-NPH) and generates an active material with the highest charge transfer resistance (0.68 Ω). In contrast, the naphthalene linker in p-NPH results in an active material with the lowest charge transfer resistance (0.20 Ω), the least negative reduction potential (−0.66 V), highest BET surface area, and the highest pseudocapacitance (292 ± 47 F/g) in the series.

Synthesis of Model Dimers. To further probe the structure-properties relationships influencing electrochemical performance in these systems, we synthesize dimer model compounds (d-BZ, d-NPH, and d-ANH) as soluble analogues for homogeneous electrochemical and spectroscopic studies (Figure 3a). The Supporting Information contains synthetic details.[15] The structures of d-BZ, d-NPH, and d-ANH were confirmed through both NMR spectroscopy and mass spectrometry

(Figures S7-9, S16-18). The alkyl chains are not removed for these studies, in contrast to the polymer synthesis, to allow for the solution-phase studies that follow. Sidechains were removed on a small sample of each dimer via thermolysis followed by mass spectrometry to confirm structure post thermolysis (Figure S19-21).

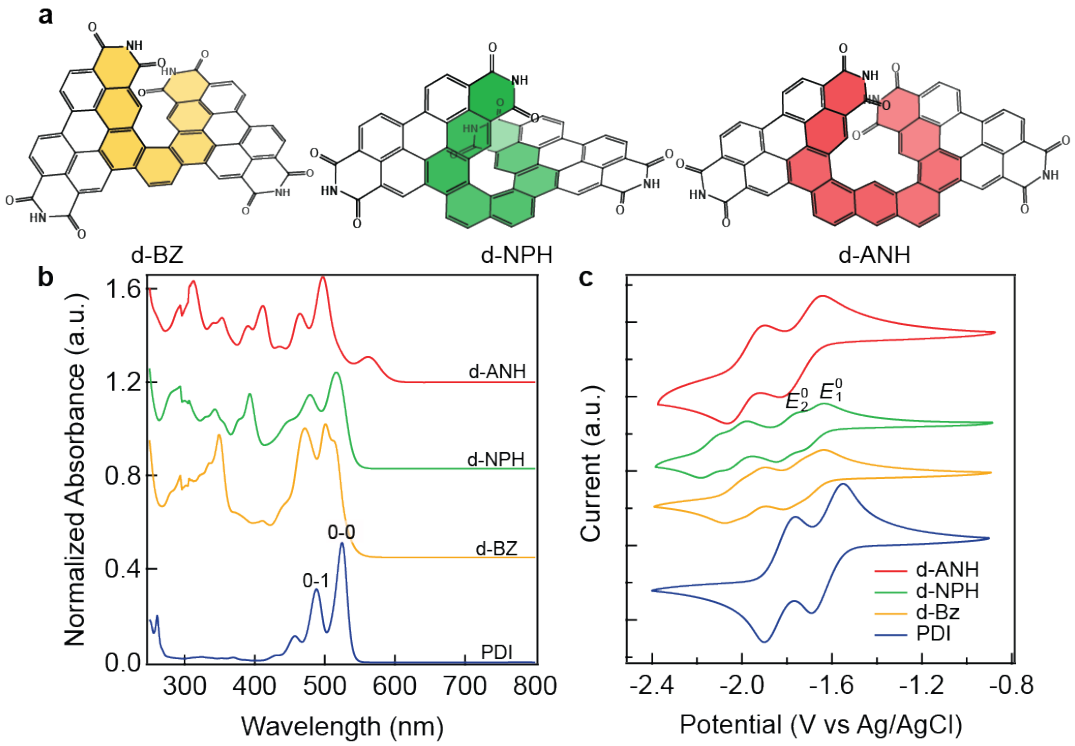

Figure 3. (a) Structures of d-BZ, -NPH, and -ANH without dodecane sidechains. Pathway between the imides to represent the PDI overlap colored in yellow, green, and red, respectively. (b) Normalized electronic absorption spectra of PDI and the PDI dimers in dichloromethane with the 0-1 and 0-0 transitions of PDI labeled. (c) Cyclic voltammograms of PDI and the PDI dimers in dichloromethane, measured at a scan rate of 50 mV/s.

Spectroscopy of Model Dimers. Figure 3b displays the electronic absorption spectra of d-BZ, d-NPH, and d-ANH in dichloromethane (PDI parent compound spectra shown for comparison, see Figure S34). PDI exhibits two characteristic peaks at 488 and 525 nm associated with $\pi - \pi^*$

electronic transitions.[16–18] The higher energy 488 nm peak represents the 0-1 vibronic transition and the lower energy 525 nm peak represents the 0-0 vibronic transition. When comparing the dimers to PDI, both the 0-0 and 0-1 peaks are blue shifted in all cases. The ratio between the absorbance of the 0-1 transition and the 0-0 transition ($\frac{A_{0-1}}{A_{0-0}}$) is used to characterize $\pi - \pi$ aggregation in heavily conjugated molecules, like perylene compounds.[16,19–21] A decrease in this ratio represents an increase in aggregation and therefore an increase in the $\pi - \pi$ interactions between molecules in solution. Here, the $A_{0\text{-}1}/A_{0\text{-}0}$ ratio decreases from d-BZ to d-ANH with a value of 0.97, 0.77 and 0.65 for d-BZ, d-NPH and d-ANH, respectively (Figure S35a). Furthermore, d-NPH experiences a red shift in the 0-0 transition when compared to d-BZ, indicating an increase in the conjugation[22] due to the NPH linker (Figure S35b). In comparison, d-ANH displays a new low energy peak at 561 nm. A previous report on d-ANH attributes this low energy absorption to anthracene-PDI intramolecular charge transfer (ICT)[18], suggesting a distinct electronic structure for this material and further highlighting the influence of linker design on material properties.

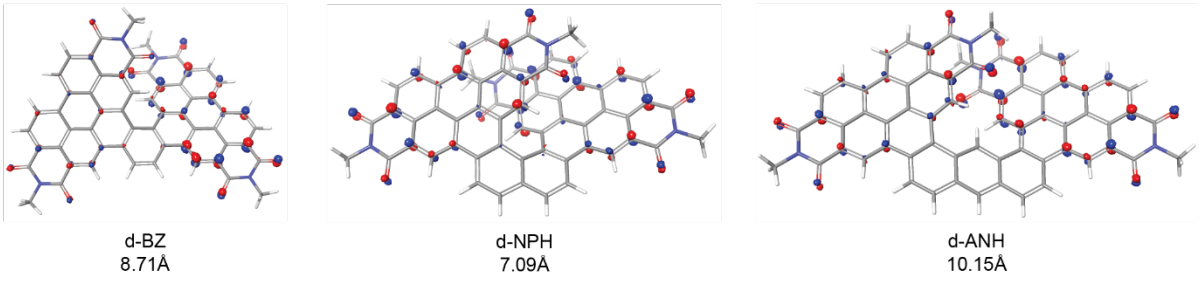

Figure 4. DFT energy minimized structures of d-BZ, -NPH, and -ANH showing the first lowest unoccupied molecular orbital (LUMO) centered on the PDI rings. Shown here is the distance between the central PDI rings (PDI-PDI distance is measured as shown in Figure S39d).

Electrochemistry of Model Dimers. To elucidate the connection between the linker structure and electron delocalization, we perform electrochemical analysis of the dimers (Figure 3c). As a proxy for electron delocalization in the reduced state, we investigate the electronic coupling through CV. To quantify the electronic coupling, the comproportionation constant (KC) can be calculated according to the following equation:

$$K_C = \exp\{[E_2^0 - E_1^0]F/RT\}$$

where E_2^0 and E_1^0 are the potential peaks labeled in the cyclic voltammogram of d-NPH (Figure 3c), F is Faraday's constant, R is the gas constant, and T is temperature. A larger value of K_C is indicative of greater electronic coupling as seen in other fully organic systems.[23–27] The CV profiles of d-BZ, d-NPH, and d-ANH exhibit four reduction waves consistent with two single-electron reductions of each PDI unit in the dimers. In agreement with a previous study on the electrochemistry of d-NPH and d-ANH[18], d-NPH displays a greater peak separation between the four single-electron redox events when compared to d-ANH. The newly synthesized d-BZ exhibits a larger peak separation than d-ANH, but overall, the cyclic voltammogram of d-NPH shows the greatest separation between the two PDI redox events and is attributed to the greatest electronic coupling across the NPH bridge. The K_C values for d-NPH and d-BZ are 158 and 40, respectively, indicating a greater degree of electronic coupling across the NPH linker. By contrast, no peak separation is observed in the voltammogram of d-ANH, suggesting negligible electronic communication across the ANH linker. The weak electronic coupling in d-ANH is consistent with the steep decline in the pseudocapacitance of p-ANH compared to the other two materials. On the other hand, d-NPH experiences both the greatest degree of electronic coupling and the highest pseudocapacitance. The electronic coupling in the dimer models is one of the various factors influencing the performance of our devices. The measured electronic coupling aligns with the trend

in the performance of our polymeric material and helps elucidate the mechanism behind the device performance.

DFT Calculations for Model Dimers. To explore this impact of linker length on the distance between the redox active PDIs, we perform density functional theory calculations on the dimer models (computational methods provided in the SI). Geometry optimization of d-BZ, d-NPH, and d-ANH result in stacked PDI units with varying degrees of PDI-PDI separation and qualitative increase of aromatic surface area depending on the linker and helical motif (Figure S36-39). These changes to the structure along the series could influence local hydrophilicity and electrolyte access to the redox active sites. However, the lowest occupied molecular orbitals shown in Figures 4 of the dimers predict that the PDI units remain the sites for reduction after coupling to these aromatic linkers. We measure the distance between the centers of adjacent PDI units as a convenient proxy for the separation between redox sites across the series. The smallest distance is calculated for d-NPH, due to favorable [6]helicene contortion, relative to the shorter d-BZ, and the largest distance between the PDI units is measured for d-ANH (Figure 4). The naphthalene linker results in the shortest distance between neighboring PDI units in the optimized dimer, which is in line with the strong electronic coupling observed in CV studies of d-NPH. These results indicate higher electronic coupling between redox sites for the d-NPH structure as a function of π-π interactions in the contorted structure rather than through bond coupling. Consequently, the calculated PDI-PDI distances also follow the trend in polymer pseudocapacitance performance.

Conclusion

In this study, we prepared a series of contorted electron accepting polymers to probe the influence of linker structure on electrochemical properties. Our results reveal key differences in the electronic structure and electrochemical performance of these active materials as the linker is

changed from benzene, to naphthalene, to anthracene. By understanding the electrochemical performance of these polymers through the prism of dimer models, we identify the degree of electronic communication between neighboring redox sites as a critical parameter influencing overall performance. The naphthalene-bridged polymer, featuring low charge-transfer resistance, a small reduction potential, higher CO_2 adsorption, and minimized spatial separation between redox units ultimately offers the best device performance in the series. As a result of these combined factors that determine device performance, we measured capacitance values of 292 ± 47 F/g for p-NPH, 250 ± 34 F/g for p-BZ, and 147 ± 18 F/g for p-ANH at a cycling rate of 0.5 A/g. Other reported organic based pseudocapacitors show values of up to 689 F/g which demonstrate the potential of this field but lack the insight gained from a fundamental study to describe design principles for these materials.[10] The recent development of PDI polymers with pseudocapacitance comparable to inorganic materials charts a path towards innovative designs, including secondary redox sites, along with further consideration of the electronic communication between these redox sites. These design principles could enable next-generation materials to out-compete inorganic counterparts, offering a new platform for economical, flexible, and adaptable energy storage solution.

ASSOCIATED CONTENT

Supporting Information. The following files are available free of charge. Synthesis of dimers and polymers, HNMR spectra, MALDI spectra, FT-IR spectra, TGA spectra, CO_2 isotherms, Electrochemical characterization, Electrode fabrication, and DFT calculations and parameters.

AUTHOR INFORMATION

Corresponding Author

***Michael L. Steigerwald** — Department of Chemistry, Columbia University, New York, New York 10027, United States; Email: mls2064@columbia.edu

***Xavier Roy** — Department of Chemistry, Columbia University, New York, New York 10027, United States; orcid.org/0000-0002-8850-0725; Email: xr2114@columbia.edu

***Colin Nuckolls** — Department of Chemistry, Columbia University, New York, New York 10027, United States; orcid.org/0000-0002-0384-5493; Email: cn37@columbia.edu

Author Contributions

†These authors contributed equally.

Notes

The authors declare no competing financial interest.

ACKNOWLEDGMENT

This work was supported by US National Science Foundation under Award no. CHE-2304946. The electrochemical measurement equipment was purchased with the help of the US Air Force Office of Scientific Research (AFOSR) Grant no. FA9550-18-1-0020. V.A.P. is supported by the

National Science Foundation Graduate Research Fellowship Program (NSF GRFP 2019279091). C.N. thanks Sheldon and Dorothea Buckler for their generous support. The authors acknowledge the use of facilities and instrumentation supported by NSF through the Columbia University, Materials Research Science and Engineering Center DMR-2011738.

ABBREVIATIONS

PDI, Perylenediimide; p-BZ, Benzene linked PDI polymer; p-NPH, Napthalene linked PDI polymer; p-ANH, Anthracene linked PDI polymer; d-BZ, Benzene linked PDI dimer; d-NPH, Napthalene linked PDI dimer; d-ANH, Anthracene linked PDI dimer.

REFERENCES

1. You, C.; Wu, X.; Yuan, X.; Chen, Y.; Liu, L.; Zhu, Y.; Fu, L.; Wu, Y.; Guo, Y.-G.; van Ree, T. Advances in Rechargeable Mg Batteries. J. Mate.r Chem. A Mater. 2020, 8 (48), 25601–25625. https://doi.org/10.1039/D0TA09330K.

2. Masias, A.; Marcicki, J.; Paxton, W. A. Opportunities and Challenges of Lithium Ion Batteries in Automotive Applications. ACS. Energy Lett. 2021, 6 (2), 621–630. https://doi.org/10.1021/acsenergylett.0c02584.

3. Xu, C.; Dai, Q.; Gaines, L.; Hu, M.; Tukker, A.; Steubing, B. Future Material Demand for Automotive Lithium-Based Batteries. Commun. Mater. 2020, 1 (1), 99. https://doi.org/10.1038/s43246-020-00095-x.

4. Choi, C.; Ashby, D. S.; Butts, D. M.; DeBlock, R. H.; Wei, Q.; Lau, J.; Dunn, B. Achieving High Energy Density and High Power Density with Pseudocapacitive Materials. Nat. Rev. Mater. 2019, 5 (1), 5–19. https://doi.org/10.1038/s41578-019-0142-z.

5. Bhojane, P. Recent Advances and Fundamentals of Pseudocapacitors: Materials, Mechanism, and Its Understanding. J. Energy Storage 2022, 45, 103654. https://doi.org/10.1016/j.est.2021.103654.

6. Fleischmann, S.; Mitchell, J. B.; Wang, R.; Zhan, C.; Jiang, D.; Presser, V.; Augustyn, V. Pseudocapacitance: From Fundamental Understanding to High Power Energy Storage Materials. Chem. Rev. 2020, 120 (14), 6738–6782. https://doi.org/10.1021/acs.chemrev.0c00170.

7. K, N.; Rout, C. S. Conducting Polymers: A Comprehensive Review on Recent Advances in Synthesis, Properties and Applications. RSC Adv. 2021, 11 (10), 5659–5697. https://doi.org/10.1039/D0RA07800J.

8. Bryan, A. M.; Santino, L. M.; Lu, Y.; Acharya, S.; D'Arcy, J. M. Conducting Polymers for Pseudocapacitive Energy Storage. Chemistry of Materials 2016, 28 (17), 5989–5998. https://doi.org/10.1021/acs.chemmater.6b01762.

9. Peurifoy, S. R.; Russell, J. C.; Sisto, T. J.; Yang, Y.; Roy, X.; Nuckolls, C. Designing Three-Dimensional Architectures for High-Performance Electron Accepting Pseudocapacitors. J. Am. Chem. Soc. 2018, 140 (35), 10960–10964. https://doi.org/10.1021/jacs.8b07365.

10. Russell, J. C.; Posey, V. A.; Gray, J.; May, R.; Reed, D. A.; Zhang, H.; Marbella, L. E.; Steigerwald, M. L.; Yang, Y.; Roy, X.; Nuckolls, C.; Peurifoy, S. R. High-Performance Organic Pseudocapacitors via Molecular Contortion. Nat Mater 2021, 20 (8), 1136–1141. https://doi.org/10.1038/s41563-021-00954-z.

11. Liu, X.; Sun, G.; Gong, Y.; Liu, C.-F.; Wang, S.; Xu, S.; Yang, X.; Yang, L.; Lai, W.-Y. Redox-Active Conjugated Microporous Polymers as Electron-Accepting Organic Pseudocapacitor

Electrode Materials for Flexible Energy Storage. Sci. China Chem. 2022, 65 (9), 1767–1774. https://doi.org/10.1007/s11426-022-1320-3.

12. Li, J.; Ballmer, S. G.; Gillis, E. P.; Fujii, S.; Schmidt, M. J.; Palazzolo, A. M. E.; Lehmann, J. W.; Morehouse, G. F.; Burke, M. D. Synthesis of Many Different Types of Organic Small Molecules Using One Automated Process. Science 2015, 347 (6227), 1221–1226. https://doi.org/10.1126/science.aaa5414.

13. Laschuk, N. O.; Easton, E. B.; Zenkina, O. V. Reducing the Resistance for the Use of Electrochemical Impedance Spectroscopy Analysis in Materials Chemistry. RSC Adv. 2021, 11 (45), 27925–27936. https://doi.org/10.1039/D1RA03785D.

14. Mei, B.-A.; Munteshari, O.; Lau, J.; Dunn, B.; Pilon, L. Physical Interpretations of Nyquist Plots for EDLC Electrodes and Devices. J. Phys. Chem. C 2018, 122 (1), 194–206. https://doi.org/10.1021/acs.jpcc.7b10582.

15. Rajasingh, P.; Cohen, R.; Shirman, E.; Shimon, L. J. W.; Rybtchinski, B. Selective Bromination of Perylene Diimides under Mild Conditions. J. Org. Chem. 2007, 72 (16), 5973–5979. https://doi.org/10.1021/jo070367n.

16. Oleson, A.; Zhu, T.; Dunn, I. S.; Bialas, D.; Bai, Y.; Zhang, W.; Dai, M.; Reichman, D. R.; Tempelaar, R.; Huang, L.; Spano, F. C. Perylene Diimide-Based Hj- and HJ-Aggregates: The Prospect of Exciton Band Shape Engineering in Organic Materials. J. Phys. Chem. C 2019, 123 (33), 20567–20578. https://doi.org/10.1021/acs.jpcc.9b04429.

17. Wang, X.; Zeng, T.; Nourrein, M.; Lai, B.-H.; Shen, K.; Wang, C.-L.; Sun, B.; Zhu, M. Concentration-Dependent Self-Assembly Structures of an Amphiphilic Perylene Diimide with

Tri(Ethylene Glycol) Substituents at Bay Positions. RSC Adv. 2017, 7 (42), 26074–26081. https://doi.org/10.1039/C7RA04296E.

18. Schuster, N. J.; Paley, D. W.; Jockusch, S.; Ng, F.; Steigerwald, M. L.; Nuckolls, C. Electron Delocalization in Perylene Diimide Helicenes. Angew. Chem., Int. Ed. 2016, 55 (43), 13519–13523. https://doi.org/10.1002/anie.201607878.

19. Margulies, E. A.; Shoer, L. E.; Eaton, S. W.; Wasielewski, M. R. Excimer Formation in Cofacial and Slip-Stacked Perylene-3,4:9,10-Bis(Dicarboximide) Dimers on a Redox-Inactive Triptycene Scaffold. Phys. Chem. Chem. Phys. 2014, 16 (43), 23735–23742. https://doi.org/10.1039/C4CP03107E.

20. Feng, J.; Zhang, Y.; Zhao, C.; Li, R.; Xu, W.; Li, X.; Jiang, J. Cyclophanes of Perylene Tetracarboxylic Diimide with Different Substituents at Bay Positions. Chem. Eur. J. 2008, 14 (23), 7000–7010. https://doi.org/10.1002/chem.200800136.

21. Adel, R.; Gala, E.; Alonso-Navarro, M. J.; Gutierrez-Fernandez, E.; Martín, J.; Stella, M.; Martinez-Ferrero, E.; de la Peña, A.; Harbuzaru, A.; Ramos, M. M.; Ortiz, R. P.; Segura, J. L.; Campoy-Quiles, M. Comparing the Microstructure and Photovoltaic Performance of 3 Perylene Imide Acceptors with Similar Energy Levels but Different Packing Tendencies. J. Mater. Chem. C Mater. 2022, 10 (5), 1698–1710. https://doi.org/10.1039/D1TC05037K.

22. Lefler, K. M.; Brown, K. E.; Salamant, W. A.; Dyar, S. M.; Knowles, K. E.; Wasielewski, M. R. Triplet State Formation in Photoexcited Slip-Stacked Perylene-3,4:9,10-Bis(Dicarboximide) Dimers on a Xanthene Scaffold. J. Phys. Chem. A 2013, 117 (40), 10333–10345. https://doi.org/10.1021/jp4083008.

23. Antoni, P. W.; Golz, C.; Hansmann, M. M. Organic Four-Electron Redox Systems Based on Bipyridine and Phenanthroline Carbene Architectures Angew. Chem., Int. Ed. 2022, 61 (24). https://doi.org/10.1002/anie.202203064.

24. Quan, M.; Sanchez, D.; Wasylkiw, M. F.; Smith, D. K. Voltammetry of Quinones in Unbuffered Aqueous Solution: Reassessing the Roles of Proton Transfer and Hydrogen Bonding in the Aqueous Electrochemistry of Quinones. J. Am. Chem. Soc. 2007, 129 (42), 12847–12856. https://doi.org/10.1021/ja0743083.

25. Chang, J.-C.; Ma, C.-J.; Lee, G.-H.; Peng, S.-M.; Yeh, C.-Y. Porphyrin–Triarylamine Conjugates: Strong Electronic Communication between Triarylamine Redox Centers via the Porphyrin Dication. Dalton Trans. 2005, No. 8, 1504–1508. https://doi.org/10.1039/B417350C.

26. Benniston, A. C.; Harriman, A.; Li, P.; Rostron, J. P.; Harrington, R. W.; Clegg, W. A Spectroscopic Study of the Reduction of Geometrically Restrained Viologens. Chem. Eur. J. 2007, 13 (28), 7838–7851. https://doi.org/10.1002/chem.200700872.

27. Hasegawa, M.; Daigoku, K.; Hashimoto, K.; Nishikawa, H.; Iyoda, M. Face-to-Face Dimeric Tetrathiafulvalenes and Their Cation Radical and Dication Species as Models of Mixed Valence and π-Dimer States. Bull. Chem. Soc. Jpn. 2012, 85 (1), 51–60. https://doi.org/10.1246/bcsj.20110224.

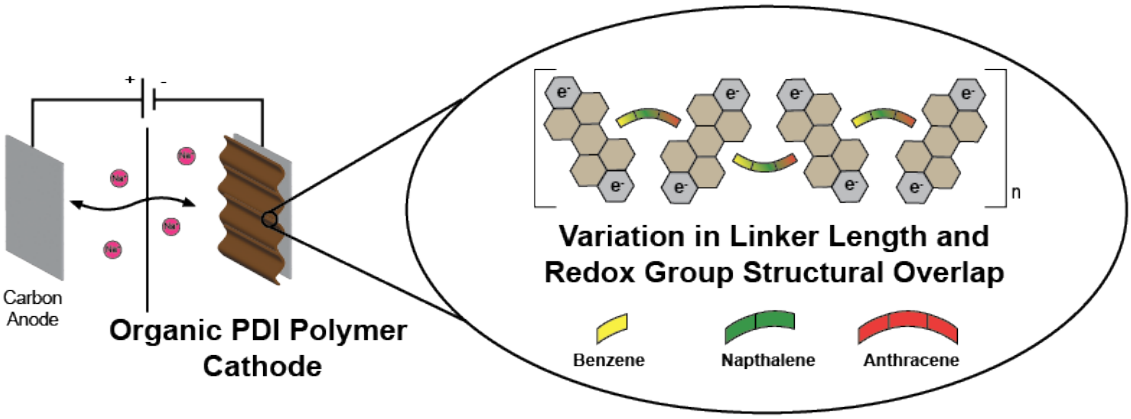
+
-
Carbon
Anode
Organic PDI Polymer
Cathode
e-
n
Variation in Linker Length and
Redox Group Structural Overlap
Benzene
Napthalene
Anthracene